



Single palladium site in ordered porous heteroatom-doped carbon for high-performance alkaline hydrogen oxidation

Haoxuan Liu^{a,b,1}, Jiantao Fu^{b,1}, Hongyi Li^{c,1}, Jiaqiang Sun^d, Xijun Liu^{a,*}, Yuan Qiu^b, Xianyun Peng^b, Yifan Liu^{e,*}, Haihong Bao^b, Longchao Zhuo^f, Rui Cao^g, Shusheng Zhang^h, Jun Luo^{b,*}

^a MOE Key Laboratory of New Processing Technology for Non-Ferrous Metals and Materials, and Guangxi Key Laboratory of Processing for Non-Ferrous Metals and Featured Materials, School of Resource, Environments and Materials, Guangxi University, Nanning 530004, China

^b Institute for New Energy Materials & Low-Carbon Technologies and Tianjin Key Lab for Photoelectric Materials & Devices, School of Materials and Engineering, Tianjin University of Technology, Tianjin 300384, China

^c Guangzhou Panyu Polytechnic, Guangzhou 511483, China

^d State Key Laboratory of Coal Conversion, Institute of Coal Chemistry, Chinese Academy of Sciences, Taiyuan 030001, China

^e College of Physics and Optoelectronic Engineering, Shenzhen University, Shenzhen 518060, China

^f School of Materials Science and Engineering, Xi'an University of Technology, Xi'an 710048, China

^g Stanford Synchrotron Radiation Light Source, SLAC National Accelerator Laboratory, Menlo Park, California 94025, United States

^h College of Chemistry, Zhengzhou University, Zhengzhou 450000, China



ARTICLE INFO

Keywords:

Alkaline hydrogen oxidation
Ordered porous carbon
Single-atomic Pd sites
Synergistic effect
Hydrogen fuel cells

ABSTRACT

Alkaline exchange membrane fuel cells are impeded by the lack of cost-effective, highly efficient catalysts for the sluggish hydrogen oxidation reaction (HOR). Herein, single-atomic Pd sites supported by ordered porous N,S-doped carbon are synthesized, exhibiting remarkable alkaline HOR performance. This catalyst exhibits an ultrahigh anodic current density and mass-specific kinetic current of 2.01 mA cm^{-2} and $27,719 \text{ A g}_{\text{Pd}}^{-1}$ (at an overpotential of 50 mV), respectively, not only outperforming the Pt/C counterpart but also making it among the best reported HOR catalysts. Furthermore, this catalyst exhibits a negligible activity decay during long-term electrolysis and a good CO tolerance capability. Experiments and theoretical calculations indicate that the synergistic effect from single Pd sites and heteroatom doping (N and S) weakens the binding energy of H_{ad} intermediates, thereby accounting for its superior HOR activity. This study provides a guideline for developing single-atomic site catalysts for highly efficient, stable alkaline HOR.

1. Introduction

Alkaline exchange membrane fuel cells (AEMFCs) have attracted immense interest in hydrogen economy due to their high energy efficiency and zero carbon emissions [1–5]. However, the kinetically sluggish anodic reaction (i.e., hydrogen oxidation reaction (HOR)) is the main bottleneck for the commercial development of AEMFCs [6,7]. Currently, Pt-based materials are the major components of anode AEMFCs catalysts toward HOR [8,9]. Thus, it is of fundamental and technological significance to improve the performance of Pt-based HOR catalysts or explore viable alternatives that exhibit high activity and cost-effectiveness for alkaline HOR (e.g., transition metals and nitrides)

[6,10–13]. Particularly, as nanoparticles and alloys, Pd has been reported to significantly promote the HOR activity in basic media [8, 14–16]. However, the high use of Pd in these Pd-based catalysts seriously limits their industry-scale applications. Furthermore, while their HOR activity is appreciable, it is subpar compared with that of Pt/C [8, 14–16]. Hence, it is imperative to explore efficient Pd-based HOR catalysts.

In recent years, single-site catalysts have demonstrated remarkable reactivity and selectivity in diverse electrocatalytic reactions due to the maximum atom-utilization efficiency and a unique local electronic structure [5,17–23]; thus, these catalysts are considered as potential successors toward HOR. Meanwhile, the performance of single-site

* Corresponding authors.

E-mail addresses: xjliu@tjut.edu.cn (X. Liu), liuyf@mail.iasf.ac.cn (Y. Liu), jluo@tjut.edu.cn (J. Luo).

¹ These authors contributed equally to this work.

catalysts is considerably dependent on support materials [24]. In this regard, an ordered porous carbon matrix is beneficial for the exposure of active sites and the mass transport of electrolytes during electrolysis [25–27]. However, to our knowledge, the combination of single-atomic Pd sites and ordered porous carbon to further promote the HOR activity of Pd-based catalysts has not been realized thus far.

Herein, single-atomic Pd sites stabilized on ordered porous N,S-doped carbon ($\text{Pd}_{\text{SA}}/\text{N},\text{S-OPC}$) were synthesized by a template-assisted wet chemical method [28,29]. Impressively, $\text{Pd}_{\text{SA}}/\text{N},\text{S-OPC}$ exhibited an excellent HOR performance and long-term stability in alkaline systems, with an ultrahigh anodic current density and a mass-specific kinetic current of 2.01 mA cm^{-2} and $27,719 \text{ A g}_{\text{Pd}}^{-1}$ (at an overpotential (η) of 50 mV), respectively; its HOR activity is not only significantly better than those of commercial Pt/C but also among the best values of previously reported HOR catalysts under equivalent conditions (Table S1). Furthermore, $\text{Pd}_{\text{SA}}/\text{N},\text{S-OPC}$ demonstrated high stability during 45-h electrocatalysis and immense tolerance toward CO poisoning. Experiments and density functional theory (DFT) simulations revealed that the efficient HOR performance is primarily related to synergistic effects from atomically dispersed Pd sites coordinated by four N atoms (namely $\text{Pd}-\text{N}_4$) and N/S dopants, collectively contributing to the optimal adsorption behavior of H_{ad} species. In addition, $\text{Pd}_{\text{SA}}/\text{N},\text{S-OPC}$ exhibited high and stable activity toward alkaline oxygen reduction reaction (ORR).

2. Experimental

2.1. Materials and methods

All chemicals (including solvents) products were analytical grade and used without further purification unless noted. The water used in all experiments was deionized (DI) water. Styrene (C_8H_8), sodium hydroxide (NaOH), polyvinylpyrrolidone (PVP), potassium persulfate ($\text{K}_2\text{S}_2\text{O}_8$), zinc nitrate hexahydrate ($(\text{Zn}(\text{NO}_3)_2 \cdot 6\text{H}_2\text{O})$, 2-methylimidazole, tetrahydrofuran (THF), trithiocyanuric acid, ammonia, and methanol were purchased from Sinopharm Chemical Reagent Co., Ltd., and palladium diacetylacetone ($\text{C}_{10}\text{H}_{14}\text{O}_4\text{Pd}$) was purchased from Alfa Aesar.

The colloidal PS was first fabricated as the precursor. Before used, styrene (50 mL) was washed thoroughly by 10 wt% NaOH solution (15 mL) and successively DI water to move the stabilizer. After that, the washed styrene was put into a 1 L triple-neck flask containing PVP (1.7 g) and DI water (400 mL), where it was bubbled using high-pure Ar for 20 min and being magnetic stirring at 92 °C for 40 min. Subsequently, 1 wt% $\text{K}_2\text{S}_2\text{O}_8$ solution (60 mL) was mixed quickly with the solution to initiate the polymerization of styrene, and then the mixture was refluxed at 92 °C under a 400 r.p.m. magnetic stirring. After waiting for 24 h, the colloidal PS dispersion was obtained. And then, 45 mL of the obtained dispersion was ultrasonicated and centrifuged for 12 h. Finally, the 3D PS templates were obtained after drying the obtained precipitations at 60 °C for 24 h.

In a typical preparation of $\text{Pd}_{\text{SA}}/\text{N},\text{S-OPC}$, the 3D PS templates (20 mg) were added in the methanol solution (150 mL) with $\text{C}_{10}\text{H}_{14}\text{O}_4\text{Pd}$ (0.1 mmol L^{-1}) under stirring for 6 h, and then dried at 60 °C under vacuum. Subsequently, the PS templates were soaked in the methanol solution (50 mL) containing $\text{Zn}(\text{NO}_3)_2 \cdot 6\text{H}_2\text{O}$ (6 g) and 2-methylimidazole (8 g) for 2 h, followed by drying under vacuum. After being immersed in the mixed solution of ammonia (30 mL) and methanol (20 mL) for 24 h, the Pd-doped ZIF-8 coated with PS (Pd-ZIF-8@PS) phase was obtained via filtering and drying. Then, the resulting Pd-ZIF-8@PS was added in THF (300 mL) and washed by centrifugation for three times to dissolve the colloidal PS and obtain the Pd-doped ordered porous single-crystalline ZIF-8 (Pd-OPC-ZIF-8). Next, the obtained Pd-OPC-ZIF-8 was heated at 120 °C under vacuum to expel residual THF. Subsequently, the powder was added into 60 mL trithiocyanuric acid solution (0.1 mol L^{-1}) followed by stirring for 60 min and drying under

vacuum for 12 h. Finally, the obtained powder was further carbonized at 1000 °C under Ar flow for 2 h to prepare $\text{Pd}_{\text{SA}}/\text{N},\text{S-OPC}$. The atomic percentages of C, N, and S in the porous carbon support are 92.27%, 6.26%, and 1.47%, respectively, examined by XPS.

For comparison, $\text{Pd}_{\text{NP}}/\text{N},\text{S-OPC}$ and $\text{Pd}_{\text{SA}}/\text{N-OPC}$ were synthesized by the same protocol as that employed for $\text{Pd}_{\text{SA}}/\text{N},\text{S-OPC}$, but with a higher content of Pd precursor or without S precursor, respectively. As for the synthesis of $\text{Pd}_{\text{SA}}/\text{PC}$, firstly, 144 mg of $\text{C}_6\text{H}_{12}\text{O}_6$ was dissolved in 40 mL ethanol, followed by adding 40 mL metal salt solution with 1.8 mg $\text{C}_{10}\text{H}_{14}\text{O}_4\text{Pd}$. After stirring at 70 °C for 16 h, the collected product was ground into fine powder. Finally, it was calcined at 600 °C at Ar atmosphere for 4 h, obtaining the final product (Pd loading: 0.25 wt%) [18,30].

2.2. Materials characterization

Powder XRD patterns of all samples were taken on a Rigaku D/max 2500 at a scan rate of $5^\circ \cdot \text{min}^{-1}$. The morphologies and structures of all samples were recorded by a field-emission SEM (Verios 460 L), a TEM equipment (Talos F200X) and a HAADF-STEM equipment (Titan Cubed Themis G2 300), all of which were equipped the energy dispersive X-ray spectroscopy (EDX). A Kratos AXIS Ultra DLD system with $\text{Al K}\alpha$ radiation as the X-ray source was performed to obtain the XPS information. The Pd amount of $\text{Pd}_{\text{SA}}/\text{N},\text{S-OPC}$, $\text{Pd}_{\text{SA}}/\text{N-OPC}$, $\text{Pd}_{\text{SA}}/\text{PC}$ and $\text{Pd}_{\text{NP}}/\text{N},\text{S-OPC}$ were analyzed by inductively coupled plasma optical emission spectrometry (ICP-OES, HORIBA Jobin Yvon, Ultima2). Nitrogen adsorption tests at 77 K were applied to measure the specific surface area using a Micromeritics Tristar II 3020 instrument. The binding energies calibration was referenced the main peak of the C 1 s at 284.8 eV. The Pd K-edge XAS spectra were performed in the transmission mode at the BL14W1 beamline station of the Shanghai Synchrotron Radiation Facility (SSRF). Please note that as for an obvious peak at near 1 Å in the FT-EXAFS spectrum of $\text{Pd}_{\text{SA}}/\text{N},\text{S-OPC}$ could be pointed to atomic X-ray absorption fine structure (AXAFS) peak, caused by scattering of the photoelectron off electrons in the periphery of the absorber atom [31].

2.3. Electrochemical measurements

All electrochemical tests were carried out on an electrochemical workstation (CHI 760E) with a standard three-electrode system under the 0.1 M KOH solution and room temperature (25 °C). A graphite rod and Hg/HgO electrode were applied as the counter electrode and reference electrode, respectively. The glassy carbon electrode loading catalyst inks were performed as the working electrode. To prepare the catalyst ink, 5 mg of the sample was dispersed in a solution containing 500 μL 0.5 wt% Nafion and 500 μL ethanol, and then the ink was dispersed by ultrasound for at least 30 min. After that, 10 μL solution was dropped at the glassy carbon electrode (0.196 cm^{-2} for the active geometric area) and dried in room temperature. The catalyst loading of $\text{Pd}_{\text{SA}}/\text{N},\text{S-OPC}$ on the glassy carbon electrode was 0.25 mg cm^{-2} . As a comparison, the $\text{Pd}_{\text{NP}}/\text{N},\text{S-OPC}$ and Pt/C electrodes were also measured.

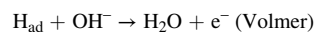
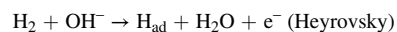
As for HOR and ORR experiments, linear sweep voltammetry (LSV) was tested with sweep rates of 1 mV s^{-1} at a rotation rate of 1600 r.p.m. in the H_2 - or O_2 -saturated electrolytes. iR compensation was applied to all initial data except stability data. All the potential values were calculated according to the equation, $E_{\text{RHE}} = E_{\text{Hg/HgO}} + E^{\text{o}}_{\text{Hg/HgO}} + 0.059 \text{ pH}$.

As for ORR, the kinetics current density (j_k) has been calculated via the following equation: $1/j_{\text{ORR,g}} = 1/j_{\text{ORR,I}} + 1/j_{\text{ORR,k}}$, where $j_{\text{ORR,g}}$ is the geometrical area-specific current density; $j_{\text{ORR,I}}$ is the limited current density; $j_{\text{ORR,k}}$ is the kinetic current density. For all the reported electrochemical results of each catalyst, the data was from three independent measurements [32,33].

2.4. Computational details

DFT calculations were performed by the Vienna Ab Initio Simulation Package (VASP), and exchange-correlation functional utilized the generalized gradient approximation (GGA) of Perdew-Becke-Ernzerhof (PBE), Bayesian Error Estimation Functional (BEEF), and revised PBE (rPBE) functionals [34]. The core electrons were symbolized with the projector-augmented wave (PAW) method. The cut-off energies for plane waves were 450 eV, providing a convergence of 10^{-5} eV in total energy and 0.02 eV/Å in Hellmann Feynman force on each atom. A Monkhorst-Pack $5 \times 5 \times 1$ k-point grid was utilized to sample the Brillouin zone for surface structure optimization. All calculations were spin-polarized due to the magnetic moment of Pd. Basic models of Pd (111) with interface surface, and Pt (111) were adopted in the computation. It should be noted that different adsorption sites (top, bridge, and hollow sites) of each model were considered to determine the optimal adsorption site.

In alkaline media, HOR is believed to proceed through either the Tafel-Volmer or the Heyrovsky-Volmer mechanism. Its elementary steps are shown in the following equations, where H_{ad} is the adsorbed hydrogen at the active site.



The H binding energies were calculated via the following equation:

$$\Delta E_{Had} = E(H_{ad}) - E(*) - \frac{1}{2} E_{H2}$$

for which $E(*)$ and $E(H_{ad})$ are the ground state energies of the clean surface and the surface with H_{ad} adsorbed, respectively. Generally, a good HOR catalyst should have a moderate hydrogen binding energy to accelerate the Volmer step.

The Gibbs free energies of H binding (ΔG_{H^*}) were obtained according to the following equation [35]:

$$\Delta G_{H^*} = [E(H_{ad}) + \Delta E_{ZPE} - T\Delta S] - E(*) - \frac{1}{2} E_{H2}$$

To correct the zero point energy (ZPE) and entropy, the ZPE and entropy corrections were made as introducing the terms of ΔE_{ZPE} and $T\Delta S$. ΔE_{ZPE} and ΔS are the corrections of zero-point energy and variation of entropy, respectively. Frequencies < 50 cm $^{-1}$ were set to 50 cm $^{-1}$.

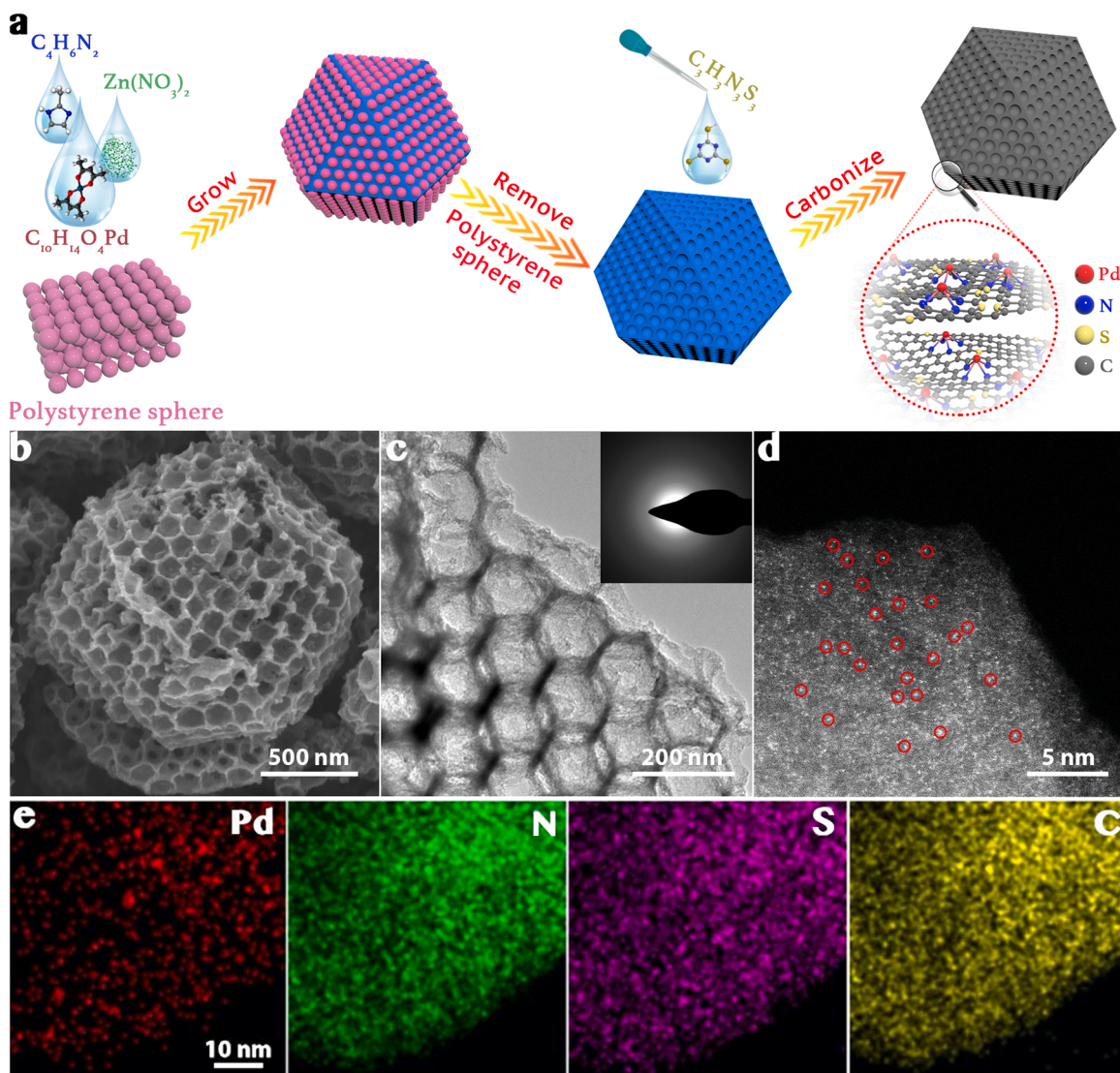


Fig. 1. Structure of Pd_{SA}/N,S-OPC. (a) Schematic of the synthetic procedure of Pd_{SA}/N,S-OPC. (b) SEM and (c) TEM images and the corresponding SAED pattern (inset of Fig. 1c) of Pd_{SA}/N,S-OPC. (d) Atomic-resolution HAADF-STEM image (partially single Pd sites indicated by red circles). (f) EDS element map distributions of Pd, N, S, and C.

E_{H_2} is the energy of one hydrogen molecule. The calculations for Bader charge and charge density were referenced to previous works [19,24].

3. Results and discussion

3.1. Synthesis and characterization of $\text{Pd}_{\text{SA}}/\text{N,S-OPC}$

The $\text{Pd}_{\text{SA}}/\text{N,S-OPC}$ catalyst was prepared by a reported method with some modifications (see details in Methods), as shown in Fig. 1a. Transmission electron microscopy (TEM) and field-emission scanning electron microscopy (SEM) images (Fig. 1b,c and S1) revealed that as-obtained $\text{Pd}_{\text{SA}}/\text{N,S-OPC}$ exhibits a highly ordered porous feature, equivalent to typical bimetallic Pd/Zn zeolitic imidazolate frameworks

(ZIF-8) [19], and this feature increases the accessibility to active sites and improves mass transport during electrolysis [25–27]. Notably, Pd nanoparticles were not clearly observed in $\text{Pd}_{\text{SA}}/\text{N,S-OPC}$ (Fig. 1c), which was in good agreement with the results obtained from X-ray diffraction (XRD): Pd-related reflection peaks were not observed (Fig. S2). In addition, the inset of selected area electron diffraction (SAED) pattern in Fig. 1c confirmed the amorphous nature of $\text{Pd}_{\text{SA}}/\text{N,S-OPC}$.

The aberration-corrected high-angle annular dark-field scanning transmission electron microscopy (HAADF-STEM) images of $\text{Pd}_{\text{SA}}/\text{N,S-OPC}$ (Fig. 1d and S3) revealed abundantly dispersed Pd sites as bright spots on the carbon matrix. In addition, this result is consistent with the above TEM and XRD results. Furthermore, the elemental mapping of

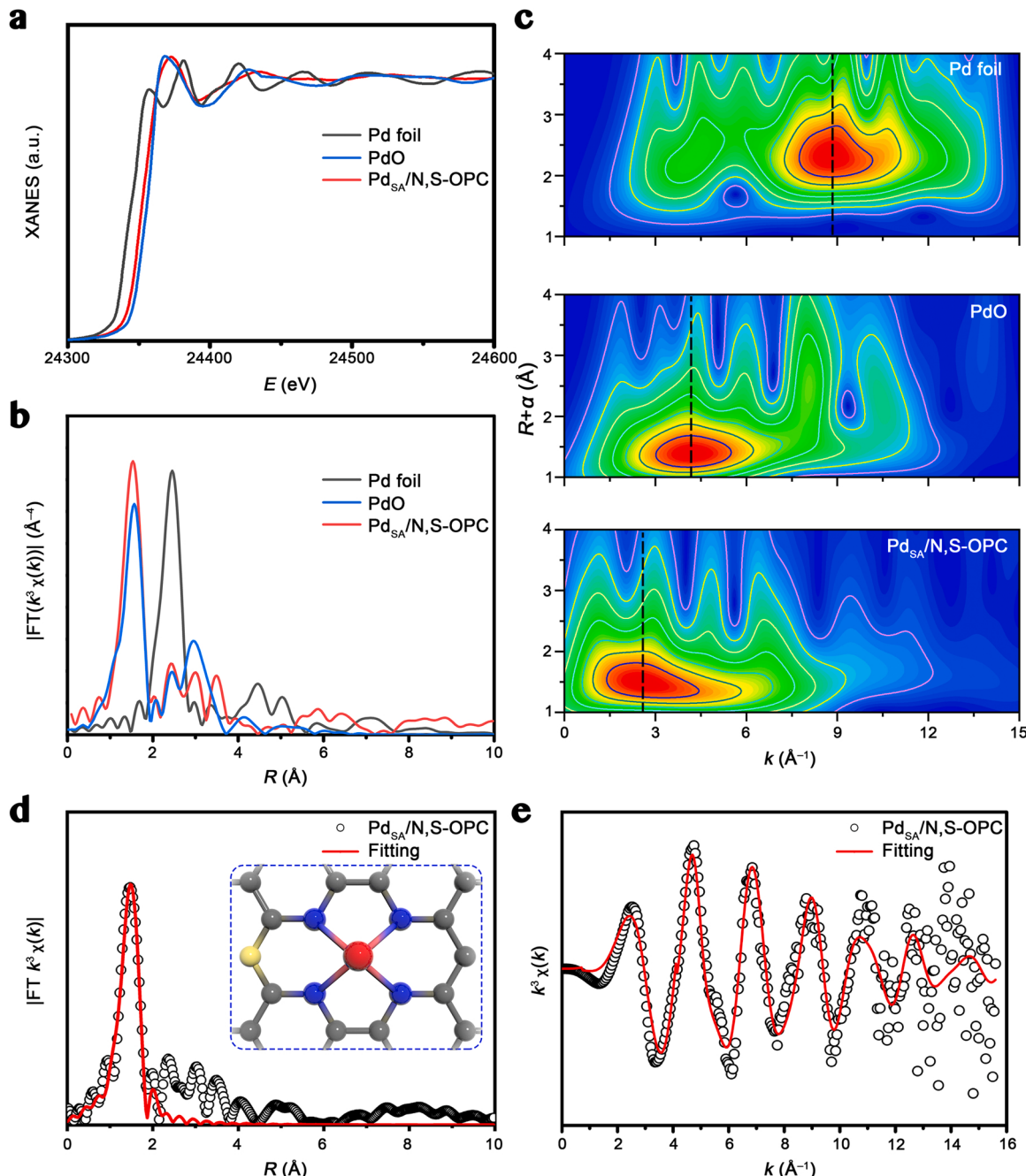


Fig. 2. Atomic structure analysis. (a) XANES and (b) FT-EXAFS curves of $\text{Pd}_{\text{SA}}/\text{N,S-OPC}$ at the Pd k -edge. (c) WT plots of Pd foil, PdO, and $\text{Pd}_{\text{SA}}/\text{N,S-OPC}$. (d, e) Corresponding model-based fittings of Pd EXAFS for $\text{Pd}_{\text{SA}}/\text{N,S-OPC}$ in R (d) and k range (e), inset shows the corresponding schematic model of $\text{Pd}_{\text{SA}}/\text{N,S-OPC}$. The peak at 0.98 Å in (d) is pointed to be the atomic XAFS.

$\text{Pd}_{\text{SA}}/\text{N,S-OPC}$ determined by energy-dispersive X-ray spectroscopy (EDS) suggested the homogenous distribution of Pd, N, and S over the entire architecture (Fig. 1e). Inductively coupled plasma atomic emission spectroscopy revealed a Pd content of up to 0.24 wt% in $\text{Pd}_{\text{SA}}/\text{N,S-OPC}$. N_2 adsorption–desorption isotherms revealed that $\text{Pd}_{\text{SA}}/\text{N,S-OPC}$ exhibits a specific surface area and microspore volume of $896.2 \text{ m}^2 \text{ g}^{-1}$ and $0.52 \text{ cm}^3 \text{ g}^{-1}$, respectively (Fig. S4). By contrast, the control sample of Pd nanoparticles (diameter: 1–3 nm) anchored to ordered porous N,S-

doped carbon ($\text{Pd}_{\text{NP}}/\text{N,S-OPC}$) with a Pd loading of 4.5 wt% was also synthesized by the same protocol as that employed for $\text{Pd}_{\text{SA}}/\text{N,S-OPC}$, but with a high content of the Pd precursor (corresponding XRD pattern and TEM images are shown in Fig. S5).

To obtain atomic structure information of $\text{Pd}_{\text{SA}}/\text{N,S-OPC}$, X-ray absorption near-edge structure (XANES) and extended X-ray absorption fine structure (EXAFS) measurements were conducted [18,19]. Fig. 2a shows the Pd K-edge XANES curves for $\text{Pd}_{\text{SA}}/\text{N,S-OPC}$ and the references

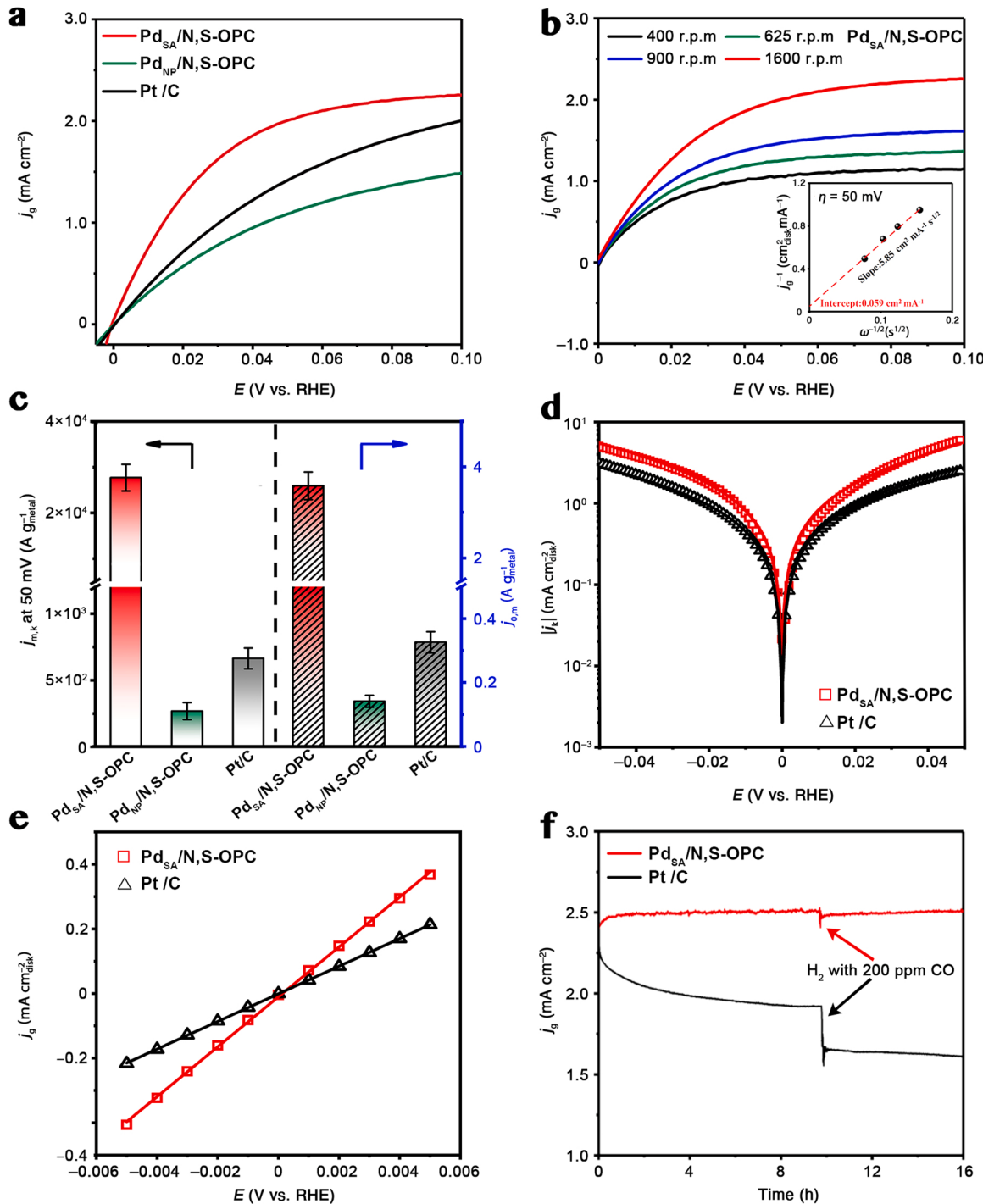


Fig. 3. Alkaline HOR performance of $\text{Pd}_{\text{SA}}/\text{N,S-OPC}$. (a) HOR polarization curves measured in an H_2 -saturated 0.1-M KOH solution at 1600 r.p.m. (b) HOR polarization curves recorded at various rotation speeds. Inset shows the K-L plot at $\eta = 50 \text{ mV}$. (c) Comparison of $j_{m,k}$ at $\eta = 50 \text{ mV}$ (unpatterned) and $j_{0,m}$. The error bars represent the standard deviations of at least three independent measurements of the same sample. (d) HOR/HER Tafel plots of j_k and corresponding Butler–Volmer fitting. (e) Micro-polarization region. (f) Chronoamperometric curves recorded in an H_2 -saturated 0.1-M KOH solution before and after the addition of 200 ppm CO at 0.2 V.

(Pd foil and PdO). The absorption edge of $\text{Pd}_{\text{SA}}/\text{N},\text{S-OPC}$ was located between Pd foil and PdO, demonstrating the average chemical state of Pd was between the two references and the Pd site exhibits positive charges [18], which is consistent with the X-ray photoelectron spectroscopy (XPS) analysis (Fig. S6). Moreover, the Fourier transform (FT) κ^3 -weighted EXAFS spectrum of $\text{Pd}_{\text{SA}}/\text{N},\text{S-OPC}$ (Fig. 2b, including the corresponding reference spectra) only revealed a primary peak at $\sim 1.5 \text{ \AA}$, corresponding to the Pd–N coordination [5]. The Pd K -edge wavelet transform (WT) EXAFS oscillations further confirmed that an intensity maximum corresponding to Pd–Pd bond was not observed in comparison with the WT plots of Pd foil and PdO (Fig. 2c). Coinciding with the HAADF-STEM characterization, all these results confirmed the atomic dispersion of the Pd sites in $\text{Pd}_{\text{SA}}/\text{N},\text{S-OPC}$ (Fig. 1d and S3).

EXAFS fitting was simultaneously conducted to characterize the quantitative structural configuration of Pd in $\text{Pd}_{\text{SA}}/\text{N},\text{S-OPC}$. Based on the fitting curves and related reports [36–41], the single Pd sites are confined with four pyridinic N atoms to form porphyrin-like moieties and exhibit a square-planar Pd–N₄ structure (Fig. 2d,e). In addition, we have also examined all other possible atomic models of $\text{Pd}_{\text{SA}}/\text{N},\text{S-OPC}$ by fitting the EXAFS result and found that Pd single atom is more likely atomically dispersed as Pd–N₄ on the N,S-doped carbon support (Fig. 2d, S7, S8, and Table S2). The strong electronic interaction between positively charged single Pd atoms and electronegative pyridinic N species, together with the large adsorption energy of Pd atomic sites to support, collectively guarantee the high stability of Pd–N₄ moieties during the electrolysis [36–38,42]. Besides, the appearance of Pd–N_x rather than Pd–C_x species in the N 1 s and C 1 s XPS spectra further confirmed that the single Pd sites in $\text{Pd}_{\text{SA}}/\text{N},\text{S-OPC}$ are stabilized by N atoms (Figs. S9 and S10), which is consistent with EXAFS fitting result (Fig. 2d) [43]. Additionally, two characteristic peaks corresponding to the C–S–C structure were observed in the high-resolution S 2p XPS spectrum (Fig. S11) [26]. Please note the inappropriate long-term storage for the single-atom catalysts, i.e., under high-temperature (over 35 °C) and high-humidity environment (70% relative humidity), maybe lead to the agglomeration of single atoms, resulting in unsatisfied electrochemical performance.

3.2. Electrocatalytic performances for alkaline HOR

Electrochemical HOR performance of $\text{Pd}_{\text{SA}}/\text{N},\text{S-OPC}$ was examined in an H₂-saturated 0.1-M KOH solution by using a rotating disk electrode. The optimal catalyst loading was 0.25 mg cm⁻² (see Fig. S12 for details). Meanwhile, 20 wt% Pt/C and $\text{Pd}_{\text{NP}}/\text{N},\text{S-OPC}$ were tested for comparison. Fig. 3a shows the linear sweep voltammetry (LSV) polarization curves of HOR on different electrodes. At a potential greater than 0 V (all potentials below were reported on the reversible hydrogen electrode (RHE), same hereafter), the anodic current of $\text{Pd}_{\text{SA}}/\text{N},\text{S-OPC}$ significantly increased with the potential, reflective of its activity toward HOR. Notably, at $\eta = 50 \text{ mV}$, $\text{Pd}_{\text{SA}}/\text{N},\text{S-OPC}$ exhibited the highest geometrical area-specific current density (j_g) of 2.01 mA cm⁻²; this value is even better than that of the Pt/C benchmark (1.42 mA cm⁻²).

Fig. 3b shows the HOR polarization curves recorded at different electrode rotation speeds: Anodic j increased with the rotation rate due to a more rapid mass transport [43]. Based on the Koutecky–Levich (K–L) equation [6], a linear correlation was obtained by fitting j_g^{-1} at $\eta = 50 \text{ mV}$ as a function of the square root of the reciprocal rotation speed ($\omega^{-1/2}$). The fitting result afforded a slope of 5.85 cm² mA⁻¹ s^{-1/2} (inset of Fig. 3b), similar to those of other HOR catalysts (for example, Ni/N-CNT, and Ni/NiO/C) and the theoretical value (4.87 cm² mA⁻¹ s^{-1/2}) [6,10]. This result revealed that the HOR catalytic behavior on $\text{Pd}_{\text{SA}}/\text{N},\text{S-OPC}$ was identical to the ideal/theoretical two-electron pathway [44]. The kinetic current density (j_k) for $\text{Pd}_{\text{SA}}/\text{N},\text{S-OPC}$ was calculated to be 16.95 mA cm⁻² for HOR at $\eta = 50 \text{ mV}$ (Fig. 3b). More strikingly, $\text{Pd}_{\text{SA}}/\text{N},\text{S-OPC}$ exhibited a substantially increased mass-specific j_k ($j_{m,k}$) 27,719 A g_{Pd}⁻¹; this value is 103 and 42 times relative to those of $\text{Pd}_{\text{NP}}/\text{N},\text{S-OPC}$ and Pt/C, respectively (Fig. 3c). To

the best of our knowledge, these two values (j_g and $j_{m,k}$ at $\eta = 50 \text{ mV}$) outperform those of most of the reported alkaline HOR catalysts (Table S1). In order to furtherly confirm the HOR activity of $\text{Pd}_{\text{SA}}/\text{N},\text{S-OPC}$, the HOR under Ar atmosphere has also been performed (Fig. S13), where no obvious HOR activity was observed compared with the test under H₂ atmosphere (Fig. 3a), demonstrating the authenticity for the superior HOR performance of $\text{Pd}_{\text{SA}}/\text{N},\text{S-OPC}$. Notably, the Pd loading content of $\text{Pd}_{\text{SA}}/\text{N},\text{S-OPC}$ was as low as 0.24 wt%, which can lead to a considerable cost reduction compared to the state-of-the-art Pt-based alkaline HOR catalysts. The results confirmed that $\text{Pd}_{\text{SA}}/\text{N},\text{S-OPC}$ is an appealing alternative to Pt-based materials.

Moreover, exchange current densities (j_0) have been calculated via fitting j_k according to the Butler–Volmer equation (Fig. 3c,d) [6]. Of note, the j_0 for $\text{Pd}_{\text{SA}}/\text{N},\text{S-OPC}$ (2.019 mA cm⁻²) was higher compared with the Pt/C counterpart (1.092 mA cm⁻²), displaying its strong intrinsic activity for HOR. Moreover, after corrected by mass, the $\text{Pd}_{\text{SA}}/\text{N},\text{S-OPC}$ showed a competitive mass-specific exchange current density ($j_{0,m}$), which was over ten-times higher than the Pt/C counterpart (Fig. 3c), furtherly confirming its outstanding HOR performance. Of note, $j_{0,m}$ value of Pt/C (0.308 A mg_{Pt}⁻¹) is consistent with literature, proving the validity of our experiment (Fig. S14 and Table S3) [45–48]. Furthermore, the symmetry factor (α) values estimated according to the Butler–Volmer equation for $\text{Pd}_{\text{SA}}/\text{N},\text{S-OPC}$ and Pt/C were 0.6 and 0.5, respectively (Table S4), all of which are very close to the theoretical value of 0.5, indicating the symmetrical HOR and HER electrocatalytic behaviors [6]. Importantly, the j_0 values were also estimated from the linear fitting of micropolarization regions (Fig. 3e) [10]. The two obtained results were almost consistent with each other (Table S3).

As the trace amount of CO in the H₂ fuel could lead to the poison for noble metals, CO tolerance capability is widely known to be crucial for evaluating the potential of an HOR catalyst for use in AEMFCs [8,10]. Clearly, compared to commercial Pt/C, $\text{Pd}_{\text{SA}}/\text{N},\text{S-OPC}$ exhibited excellent tolerance to CO crossover (Fig. 3f). An accelerated durability test was conducted to assess the stability of $\text{Pd}_{\text{SA}}/\text{N},\text{S-OPC}$. When operating the HOR test at a constant potential of 0.1 V, 82.7% of the current density was maintained for $\text{Pd}_{\text{SA}}/\text{N},\text{S-OPC}$ after 45-h (Fig. S15); this value is better than that observed for Pt/C (50.8% for 30 h). Besides, the reusability of $\text{Pd}_{\text{SA}}/\text{N},\text{S-OPC}$ was further evaluated by potential cycling: A slight decay in the activity after 3000 cyclic voltammetry cycles was noted (Fig. S16), demonstrating its excellent electrocatalytic reusability. Furthermore, an additional XPS result, XRD patterns, and HAADF-STEM images have confirmed that the single-atomic Pd sites on $\text{Pd}_{\text{SA}}/\text{N},\text{S-OPC}$ are well preserved (Figs. S17–S19), demonstrating its superior chemical and structure stability.

3.3. DFT-calculations and HOR mechanism

To understand the nature of efficient HOR reaction kinetics of $\text{Pd}_{\text{SA}}/\text{N},\text{S-OPC}$, DFT calculations were performed (see details in Methods). Recent studies demonstrated that alkaline HOR process follows a Tafel–Volmer or Heyrovsky–Volmer mechanism [1,11], both of which indicate the Volmer step ($\text{H}_{\text{ad}} + \text{OH}^- \rightarrow \text{H}_2\text{O} + \text{e}^-$) is the rate-determining step because of its strong hydrogen binding energy (HBE), particularly for metal catalysts (for example, Ni and Pd) [10–12,49]. As suggested by Sabatier's principle, the binding energy of H_{ad} should not be too strong or too weak for a good HOR catalyst [49]. Fig. 4a depicts the optimal adsorption structure with H_{ad} intermediate on $\text{Pd}_{\text{SA}}/\text{N},\text{S-OPC}$ surface. And, the hydrogen binding energy (ΔE_{H}) by using BEEF functional [50] of $\text{Pd}_{\text{SA}}/\text{N},\text{S-OPC}$ was found to be 0.285 eV (Fig. S20); this value is considerably greater than those of Pt (111) (-0.424 eV) and Pd (111) (-0.515 eV), suggestive of a decreased binding strength of H on $\text{Pd}_{\text{SA}}/\text{N},\text{S-OPC}$ surface. Furtherly, the Gibbs free energies of adsorbed H^* (ΔG_{H^*}) for $\text{Pd}_{\text{SA}}/\text{N},\text{S-OPC}$, Pd(111) and Pt(111) have been calculated (Fig. 4b). Obviously, the ΔG_{H^*} value of $\text{Pd}_{\text{SA}}/\text{N},\text{S-OPC}$ is closest to zero, providing both a faster proton/electron-transfer step and hydrogen adsorb/release process. This usually implies a better HOR performance, which is also in

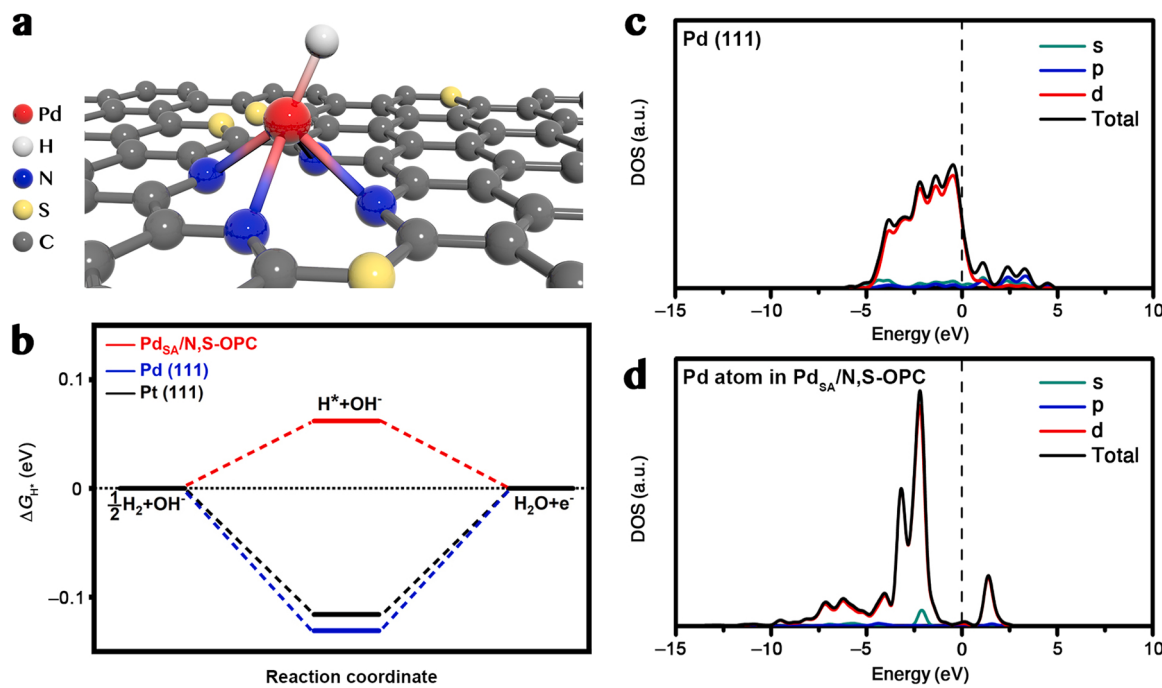


Fig. 4. DFT calculations. (a) Optimized adsorption configuration on Pd_{SA}/N,S-OPC of H_{ad}. (b) Calculated ΔG_{H^*} on different catalyst surfaces. Calculated DOS curves for Pd (111) (c) and Pd_{SA}/N,S-OPC (d). The Pd (111) model is selected because Fig. S5 indicates that the preferential orientation of Pd NP in Pd_{NP}/N,S-OPC is <111>.

agreement with the above experiments (Fig. 3a). Meantime, the calculated ΔE_H results with rPBE and PBE functionals [51,52] also confirmed the optimal adsorptive behavior over Pd_{SA}/N,S-OPC (Fig. S20).

Moreover, the location of *d* orbital has been applied to examine the catalytic kinetic activity [53–56]. As illustrated by the density of states (DOS) in Fig. 4c,d, the *d* orbital of Pd_{SA}/N,S-OPC is downshifted from the Fermi level, which is associated with a weak HBE, thus facilitating the desorption of H_{ad} from catalyst surface for HOR. All these results evidenced that incorporating single Pd sites into the N,S-doped carbon is an efficient strategy to weaken the HBE and consequently to support an enhanced HOR performance.

To explore the role of the N and S dopants in Pd_{SA}/N,S-OPC, control samples comprising single-atomic Pd sites anchored to N-doped ordered porous carbon (represented as Pd_{SA}/N-OPC) or PC without any dopants (represented as Pd_{SA}/PC) were prepared (Figs. S21–S24). Of note, Pd loading contents of Pd_{SA}/N,S-OPC, Pd_{SA}/N-OPC, and Pd_{SA}/PC are 0.24, 0.24, and 0.25 wt%, respectively. The EXAFS fitting result revealed that the single Pd sites in Pd_{SA}/N-OPC exist as Pd–N₄ moieties (Fig. S23). Notably, the HOR catalytic activity followed a sequence of Pd_{SA}/PC < Pd_{SA}/N-OPC < Pd_{SA}/N,S-OPC (Figs. S25–S27 and Table S4). The calculated ΔE_H values of Pd_{SA}/N-OPC and Pd_{SA}/PC were 1.824 eV and 0.791 eV, respectively; the two values are clearly greater than that of Pd_{SA}/N,S-OPC (Fig. S28). The much weakened HBE on the Pd_{SA}/N-OPC and Pd_{SA}/PC surfaces make it not favorable for the capture of the H_{ad} species to produce H₂O according to the Volmer step, leading to inferior alkaline HOR activity [11]. According to previous studies [30,36–38,42,57], the introduction of N atoms plays a crucial role in stabilizing single Pd atoms and modifying the electronic properties of neighboring Pd atoms. Moreover, although the S atoms do not be directly connected with the single Pd atoms, they also can influence the electronic structure of Pd atoms [58–60]. As shown in Figs. S29–S31, when S dopant was also introduced to Pd_{SA}/N-OPC, the local charge density of Pd single atom and its adjacent N atoms furtherly increased, benefitting to capture H_{ad} and easier strating the rate-determining Volmer step, thus leading to an enhanced HOR performance [61]. Overall, the combination of experimental and calculation results collectively confirmed that the presence of single-atomic Pd–N₄ moieties and codoping with

heteroatoms (i.e., N and S) synergistically decreases the HBE, accounting for the efficient HOR performance of Pd_{SA}/N,S-OPC.

In addition to the high efficiency and durability for HOR, Pd_{SA}/N,S-OPC was an efficient electrocatalyst for alkaline ORR (Fig. S32). A half-wave potential ($E_{1/2}$) of 0.85 V for ORR is achieved on Pd_{SA}/N,S-OPC; this value is superior to those of Pd_{SA}/N-OPC (0.73 V) and Pd_{NP}/N,S-OPC (0.77 V) and same as that of Pt/C (0.86 V) (Fig. S32a, d). In order to express the instinct ORR activity of Pd_{SA}/N,S-OPC, its kinetics current densities and corresponding mass-normalized value ($j_{ORR,k}$ and $j_{ORR,m,k}$) have been calculated to be 4.583 mA cm⁻² and 3818.9 A mg_{Pt}⁻¹, respectively, which are close to or even surpass the Pt/C counterparts (6.024 mA cm⁻² and 150.6 A mg_{Pt}⁻¹), demonstrating its superior instinct activity for ORR (Fig. S32c). Besides, Pd_{SA}/N,S-OPC also exhibited outstanding stability and Pt/C-surpassed CO-tolerance toward ORR (Figs. S32 and S33) [30], and its structure stability has been confirmed by the corresponding HAADF-STEM images recorded after the long-term ORR electrocatalysis (Fig. S34). These results demonstrated that Pd_{SA}/N,S-OPC is a versatile catalyst in diverse electrochemical reactions.

4. Conclusion

In summary, single-atomic Pd dispersed on ordered porous N,S-doped carbon was rationally developed, and the resulting catalyst exhibited an outstanding HOR activity in alkaline media, with the anodic current density and mass-specific kinetic current of 2.01 mA cm⁻² and 27,719 A g_{Pd}⁻¹, respectively; these results manifesting one of the best alkaline HOR catalysts. Meantime, experiments combined with DFT calculations revealed that the strong synergistic effect between single-atomic Pd sites and N,S-doped carbon substance can boost HOR activity due to the optimal adsorptive behavior of H_{ad} intermediates. In addition, the hierarchically ordered porous structure in N,S-doped carbon provides more accessible active sites and more efficient mass transfer. To further improve the HOR specific activity of Pd_{SA}/N,S-OPC sample, furtherly tuning the electronic property and surrounding environment of isolated metal atoms via doping heteroatoms is suggested. We believe that the present study can shed light on the development of highly efficient, low-cost single-site catalysts for

alkaline hydrogen fuel cells.

Authors contribution

X.J.L. designed the electrocatalysts. **H.X.L.** performed the synthetic experiments and the characterizations of electrocatalysts. **J.T.F.** performed the electrochemical experiments, and analyzed the electrochemical data, to which **Y.Q.** and **X.Y.P.** contributed. **H.Y.L.** and **Y.F.L.** co-performed the calculations and XAS characterizations and analyzed their results, to which **H.H.B.** and **R.C.** assisted. **L.C.Z.**, **J.Q.S.** and **S.S.Z.** assisted in the characterizations of electrocatalysts. **X.J.L.** and **J.L.** co-performed the mechanism analysis and co-wrote the paper, to which **H.X.L.** contributed. **X.J.L.**, **Y.F.L.** and **J.L.** co-supervised this project. All authors discussed the results. All authors discussed the results and implications at all stages.

CRediT authorship contribution statement

Haoxuan Liu: Data curation, Methodology, Investigation, Writing – review & editing. **Jiantao Fu:** Data curation, Methodology. **Hongyi Li:** Data curation, Methodology, Editing. **Jiaqiang Sun:** Data curation, Methodology. **Xijun Liu:** Conceptualization, Project administration, Supervision. **Yuan Qiu:** Methodology, review & editing. **Xianyun Peng:** Methodology, review & editing. **Yifan Liu:** Methodology, Supervision. **Haihong Bao:** Data curation, Methodology. **Longchao Zhuo:** Data curation, Methodology. **Rui Cao:** Data curation, Methodology. **Shusheng Zhang:** Data curation, Methodology. **Jun Luo:** Project administration, review & editing.

Declaration of Competing Interest

The authors declare that they have no known competing financial interests or personal relationships that could have appeared to influence the work reported in this paper.

Acknowledgments

This work was financially supported by National Natural Science Foundation of China (51971157, 22075211, 21601136, and 51621003), the Tianjin Science Fund for Distinguished Young Scholars (19JCJQJC61800), and the Guangzhou Panyu Polytechnic Science & Technology Project No. 2021KJ01. The authors also acknowledged Beijing Super Cloud Computing Center for providing the computational resources.

Appendix A. Supporting information

Supplementary data associated with this article can be found in the online version at [doi:10.1016/j.apcatb.2021.121029](https://doi.org/10.1016/j.apcatb.2021.121029).

References

- [1] D. Strmcnik, M. Uchimura, C. Wang, R. Subbaraman, N. Danilovic, D. Van Der Vliet, A.P. Paulikas, V.R. Stamenkovic, N.M. Markovic, Improving the hydrogen oxidation reaction rate by promotion of hydroxyl adsorption, *Nat. Chem.* 5 (2013) 300–306.
- [2] J. Zheng, W. Sheng, Z. Zhuang, B. Xu, Y. Yan, Universal dependence of hydrogen oxidation and evolution reaction activity of platinum-group metals on pH and hydrogen binding energy, *Sci. Adv.* 2 (2016), e1501602.
- [3] Y. Wang, G. Wang, G. Li, B. Huang, J. Pan, Q. Liu, J. Han, L. Xiao, J. Lu, L. Zhuang, Pt–Ru catalyzed hydrogen oxidation in alkaline media: Oxophilic effect or electronic effect? *Energy Environ. Sci.* 8 (2015) 177–181.
- [4] J. Lilloja, E. Kibena-Pöldsepp, A. Sarapuu, A. Kikas, V. Kisand, M. Käärik, M. Merisalu, A. Treshchalov, J. Leis, V. Sammelselg, Q. Wei, S. Holdcroft, K. Tammeveski, Nitrogen-doped carbide-derived carbon/carbon nanotube composites as cathode catalysts for anion exchange membrane fuel cell application, *Appl. Catal. B* 272 (2020), 119012.
- [5] Y. Chen, S. Ji, S. Zhao, W. Chen, J. Dong, W.-C. Cheong, R. Shen, X. Wen, L. Zheng, A.I. Rykov, S. Cai, H. Tang, Z. Zhuang, C. Chen, Q. Peng, D. Wang, Y. Li, Enhanced oxygen reduction with single-atomic-site iron catalysts for a zinc-air battery and hydrogen-air fuel cell, *Nat. Commun.* 9 (2018) 5422.
- [6] Z. Zhuang, S.A. Giles, J. Zheng, G.R. Jenness, S. Caratzoulas, D.G. VLachos, Y. Yan, Nickel supported on nitrogen-doped carbon nanotubes as hydrogen oxidation reaction catalyst in alkaline electrolyte, *Nat. Commun.* 7 (2016) 10141.
- [7] G. Wang, W. Li, N. Wu, B. Huang, L. Xiao, J. Lu, L. Zhuang, Unraveling the composition-activity relationship of PtRu binary alloy for hydrogen oxidation reaction in alkaline media, *J. Power Sources* 412 (2019) 282–286.
- [8] Y. Cong, B. Yi, Y. Song, Hydrogen oxidation reaction in alkaline media: from mechanism to recent electrocatalysts, *Nano Energy* 44 (2018) 288–303.
- [9] S. Lu, Z. Zhuang, Investigating the influences of the adsorbed species on catalytic activity for hydrogen oxidation reaction in alkaline electrolyte, *J. Am. Chem. Soc.* 139 (2017) 5156–5163.
- [10] A. Lim, J. Kim, H.-J. Lee, H.-J. Kim, S.J. Yoo, J.H. Jang, H.Y. Park, Y.-E. Sung, H. S. Park, Low-loading IrO₂ supported on Pt for catalysis of PEM water electrolysis and regenerative fuel cells, *Appl. Catal. B* 272 (2020), 118955.
- [11] F. Yang, X. Bao, P. Li, X. Wang, G. Cheng, S. Chen, W. Luo, Boosting hydrogen oxidation activity of Ni in alkaline media through oxygen-vacancy-rich CeO₂/Ni heterostructures, *Angew. Chem. Int. Ed.* 58 (2019) 14179–14183.
- [12] T. Wang, M. Wang, H. Yang, M. Xu, C. Zuo, K. Feng, M. Xie, J. Deng, J. Zhong, W. Zhou, T. Cheng, Y. Li, Weakening hydrogen adsorption on nickel via interstitial nitrogen doping promotes bifunctional hydrogen electrocatalysis in alkaline solution, *Energy Environ. Sci.* 12 (2019) 3522–3529.
- [13] W. Ni, A. Krammer, C. Hsu, H.M. Chen, A. Schueler, X. Hu, Ni₃N as an active hydrogen oxidation reaction catalyst in alkaline medium, *Angew. Chem. Int. Ed.* 58 (2019) 7445–7449.
- [14] H. Yu, E.S. Davydova, U. Ash, H.A. Miller, L. Bonville, D.R. Dekel, R. Maric, Palladium-ceria nanocatalyst for hydrogen oxidation in alkaline media: optimization of the Pd–CeO₂ interface, *Nano Energy* 57 (2019) 820–826.
- [15] M. Alesker, M. Page, M. Shviro, Y. Paska, G. Gershinsky, D.R. Dekel, D. Zitoun, Palladium/nickel bifunctional electrocatalyst for hydrogen oxidation reaction in alkaline membrane fuel cell, *J. Power Sources* 304 (2016) 332–339.
- [16] S.S. John, I.R.W. Atkinson, K.A. Unocic, R.R. Unocic, J.T.A. Zawodzinski, A. B, Platinum and palladium overlayers dramatically enhance the activity of ruthenium nanotubes for alkaline hydrogen oxidation, *ACS Catal.* 5 (2015) 7015–7023.
- [17] L. Zhang, L. Han, H. Liu, X. Liu, J. Luo, Potential-cycling synthesis of single platinum atoms for efficient hydrogen evolution in neutral media, *Angew. Chem. Int. Ed.* 56 (2017) 13694–13698.
- [18] L. Han, X. Liu, J. Chen, R. Lin, H. Liu, F. Lü, S. Bak, Z. Liang, S. Zhao, E. Stavitski, J. Luo, R.R. Adzic, H.L. Xin, Atomically dispersed molybdenum catalysts for efficient ambient nitrogen fixation, *Angew. Chem. Int. Ed.* 58 (2019) 2321–2325.
- [19] F. Lü, S. Zhao, R. Guo, J. He, X. Peng, H. Bao, J. Fu, L. Han, G. Qi, J. Luo, X. Tang, X. Liu, Nitrogen-coordinated single Fe sites for efficient electrocatalytic N₂ fixation in neutral media, *Nano Energy* 61 (2019) 420–427.
- [20] L. Wang, X. Duan, X. Liu, J. Gu, R. Si, Y. Qiu, D. Shi, F. Chen, X. Sun, J. Lin, J. Sun, Atomically dispersed Mo supported on metallic Co₉S₈ nanoflakes as an advanced noble-metal-free bifunctional water splitting catalyst working in universal pH conditions, *Adv. Energy Mater.* 4 (2019) 1903137.
- [21] Z. Chen, E. Vorobyeva, S. Mitchell, E. Fako, M.A. Ortúñoz, N. López, S.M. Collins, P. A. Midgley, S. Richard, G. Vilé, J. Pérez-Ramírez, A heterogeneous single-atom palladium catalyst surpassing homogeneous systems for Suzuki coupling, *Nat. Nanotechnol.* 13 (2018) 702–707.
- [22] Q. Wang, S. Santos, C.A. Urbina-Blanco, W.Y. Hernández, M. Impérator-Clerc, E. I. Vok, M. Marinova, O. Ersen, W. Baaziz, O.V. Safonova, A.Y. Khodakov, M. Saefs, V.V. Ordovsky, Solid micellar Ru single-atom catalysts for the water-free hydrogenation of CO₂ to formic acid, *Appl. Catal. B* 290 (2020), 120036.
- [23] W. Ni, Z. Liu, X. Guo, Y. Zhang, C. Ma, Y. Deng, S. Zhang, Dual single-cobalt atom-based carbon electrocatalysts for efficient CO₂-to-syngas conversion with industrial current densities, *Appl. Catal. B* 291 (2021), 120092.
- [24] D. Zhao, Z. Chen, W. Yang, S. Liu, X. Zhang, Y. Yu, W.-C. Cheong, L. Zheng, F. Ren, G. Ying, X. Cao, D. Wang, Q. Peng, G. Wang, C. Chen, MXene (Ti₃C₂) vacancy-confined single-atom catalyst for efficient functionalization of CO₂, *J. Am. Chem. Soc.* 141 (2019) 4086–4093.
- [25] M. Qiao, Y. Wang, Q. Wang, G. Hu, X. Mamat, S. Zhang, S. Wang, Hierarchically ordered porous carbon with atomically dispersed FeN₄ for ultra-efficient oxygen reduction reaction in proton-exchange membrane fuel cells, *Angew. Chem. Int. Ed.* 59 (2020) 2688–2694.
- [26] K. Wu, X. Chen, S. Liu, Y. Pan, W.-C. Cheong, W. Zhu, X. Cao, R. Shen, W. Chen, J. Luo, W. Yan, L. Zheng, Z. Chen, D. Wang, Q. Peng, C. Chen, Y. Li, Porphyrin-like Fe-N₄ sites with sulfur adjustment on hierarchical porous carbon for different rate-determining steps in oxygen reduction reaction, *Nano Res.* 11 (2018) 6260–6269.
- [27] W. Wan, X. Liu, H. Li, X. Peng, D. Xi, J. Luo, 3D carbon framework-supported CoNi nanoparticles as bifunctional oxygen electrocatalyst for rechargeable Zn-air batteries, *Appl. Catal. B* 240 (2019) 193–200.
- [28] T.F. Baumann, J.H. Satcher, Homogeneous incorporation of metal nanoparticles into ordered macroporous carbons, *Chem. Mater.* 15 (2003) 3745–3747.
- [29] H. Hong, J. Liu, H. Huang, C.A. Etogo, X. Yang, B. Guan, L. Zhang, Ordered macro-microporous metal–organic framework single crystals and their derivatives for rechargeable aluminum-ion batteries, *J. Am. Chem. Soc.* 141 (2019) 14764–14771.
- [30] P. Weber, M. Werheid, M. Janssen, M. Oezaslan, Fundamental insights in degradation mechanisms of Pt/C nanoparticles for the ORR, *ECS Trans.* 86 (2018) 433–445.
- [31] D.E. Ramaker, B.L. Mojat, D.C. Koningsberger, W.E. O’Grady, Understanding atomic X-ray absorption fine structure in X-ray absorption spectra, *J. Phys. Condens. Matter* 10 (1998) 8753–8770.

- [32] F. Hasché, M. Oezaslan, P. Strasser, Activity, stability, and degradation mechanisms of dealloyed PtCu₃ and PtCo₃ nanoparticle fuel cell catalysts, *ChemCatChem* 3 (2011) 1805–1813.
- [33] M. Luo, Z. Zhao, Y. Zhang, Y. Sun, Y. Xing, F. Lv, Y. Yang, X. Zhang, S. Hwang, Y. Qin, J. Ma, F. Lin, D. Su, G. Lu, S. Guo, PdMo bimetallene for oxygen reduction catalysis, *Nature* 574 (2019) 81–85.
- [34] A.J.R. Hensley, K. Ghale, C. Rieg, T. Dang, E. Anderst, F. Studt, C.T. Campbell, J.-S. McEwen, Y. Xu, DFT-based method for more accurate adsorption energies: an adaptive sum of energies from RPBE and vdW density functionals, *J. Phys. Chem. C* 121 (2017) 4937–4945.
- [35] K. Hu, T. Ohto, Y. Nagata, M. Wakisaka, Y. Aoki, J.-I. Fujita, Y. Ito, Catalytic activity of graphene-covered non-noble metals governed by proton penetration in electrochemical hydrogen evolution reaction, *Nat. Commun.* 12 (2021) 203.
- [36] D.A. Bulushev, M. Zacharska, E.V. Shlyakhova, A.L. Chuvalin, Y. Guo, S. Beloshapkin, A.V. Okotrub, L.G. Bulusheva, Single isolated Pd²⁺ cations supported on N-doped carbon as active sites for hydrogen production from formic acid decomposition, *ACS Catal.* 6 (2016) 681–691.
- [37] A. Wang, J. Li, T. Zhang, Heterogeneous single-atom catalysis, *Nat. Rev. Chem.* 2 (2018) 65–81.
- [38] H. Fei, J. Dong, Y. Feng, C. Allen, C. Wan, B. Volosskiy, M. Li, Z. Zhao, Y. Wang, H. Sun, P. An, W. Chen, Z. Guo, C. Lee, D. Chen, I. Shakir, M. Liu, T. Hu, Y. Li, A. Kirkland, X. Duan, Y. Huang, General synthesis and definitive structural identification of MN₄C₄ single-atom catalysts with tunable electrocatalytic activities, *Nat. Catal.* 1 (2018) 63–72.
- [39] A. Zitolo, V. Goellner, V. Armel, M.-T. Sougrati, T. Mineva, L. Stievano, E. Fonda, F. Jaouen, Identification of catalytic sites for oxygen reduction in iron- and nitrogen-doped graphene materials, *Nat. Mater.* 14 (2015) 937–942.
- [40] E.A. Stern, D.E. Sayers, F.W. Lytle, Extended x-ray-absorption fine-structure technique. III. Determination of physical parameters, *Phys. Rev. B* 11 (1975) 4836–4846.
- [41] S. Zhou, L. Shang, Y. Zhao, R. Shi, G.I.N. Waterhouse, Y. Huang, L. Zheng, T. Zhang, Pd single-atom catalysts on nitrogen-doped graphene for the highly selective photothermal hydrogenation of acetylene to ethylene, *Adv. Mater.* 31 (2019) 1900509.
- [42] Q. Liu, Y. Li, L. Zheng, J. Shang, X. Liu, R. Yu, J. Shui, Sequential synthesis and active-site coordination principle of precious metal single-atom catalysts for oxygen reduction reaction and PEM fuel cells, *Adv. Energy Mater.* 10 (2020) 2000689.
- [43] H. Li, L. Zhang, L. Li, C. Wu, Y. Huo, Y. Chen, X. Liu, X. Ke, J. Luo, G. Van Tendeloo, Two-in-one solution using insect wings to produce graphene-graphite films for efficient electrocatalysis, *Nano Res.* 12 (2019) 33–39.
- [44] W. Sheng, H.A. Gasteiger, S.-H. Yang, Hydrogen oxidation and evolution reaction kinetics on platinum: acid vs alkaline electrolytes, *J. Electrochem. Soc.* 157 (2010) B1529–B1536.
- [45] Q. Li, H. Peng, Y. Wang, L. Xiao, J. Lu, L. Zhuang, The comparability of Pt to Pt-Ru in catalyzing the hydrogen oxidation reaction for alkaline polymer electrolyte fuel cells operated at 80 °C, *Angew. Chem. Int. Ed.* 58 (2019) 1442–1446.
- [46] S.M. Alia, B.S. Pivovar, Y. Yan, Platinum-coated copper nanowires with high activity for hydrogen oxidation reaction in base, *J. Am. Chem. Soc.* 135 (2013) 13473–13478.
- [47] S.M. Alia, B.S. Pivovar, Evaluating hydrogen evolution and oxidation in alkaline media to establish baselines, *J. Electrochem. Soc.* 165 (2018) F441–F455.
- [48] C. Wei, R.R. Rao, J. Peng, B. Huang, I.E.L. Stephens, M. Risch, Z.J. Xu, Y. Shao-Horn, Recommended practices and benchmark activity for hydrogen and oxygen electrocatalysis in water splitting and fuel cells, *Adv. Mater.* 31 (2019) 1806296.
- [49] X. Qin, L. Zhang, G.-L. Xu, S. Zhu, Q. Wang, M. Gu, X. Zhang, C.-J. Sun, P. B. Balbuena, K. Amine, M. Shao, The role of Ru in improving the activity of Pd toward hydrogen evolution and oxidation reactions in alkaline solutions, *ACS Catal.* 9 (2019) 9614–9621.
- [50] J. Wellendorff, K. Lundgaard, A. Møgelhøj, V. Petzold, D. Landis, J. Nørskov, T. Bligaard, K. Jacobsen, Density functionals for surface science: exchange-correlation model development with Bayesian error estimation, *Phys. Rev. B* 85 (2012), 235149.
- [51] B. Hammer, L.B. Hansen, J.K. Nørskov, Improved adsorption energetics within density-functional theory using revised Perdew-Burke-Ernzerhof functionals, *Phys. Rev. B* 59 (1999) 7413–7421.
- [52] J.L. Nie, L. Ao, X.T. Zu, Modeling the electrochemical hydrogen oxidation and evolution reactions on the basis of density functional theory calculations, *Mod. Phys. Lett. B* 29 (2015) 1550199.
- [53] Z. Jakub, J. Hulya, M. Meier, R. Bliem, F. Kraushofer, M. Setvin, M. Schmid, U. Diebold, C. Franchini, G.S. Parkinson, Local structure and coordination define adsorption in a model Ir₁/Fe₃O₄ single-atom catalyst, *Angew. Chem. Int. Ed.* 58 (2019) 13961–13968.
- [54] M.T. Greiner, T.E. Jones, S. Beeg, L. Zwiener, M. Scherzer, F. Girsidis, S. Piccinin, M. Armbrüster, A. Knop-Gericke, R. Schlögl, Free-atom-like d states in single-atom alloy catalysts, *Nat. Chem.* 10 (2018) 1008–1015.
- [55] L. Xiong, B. Wang, H. Cai, H. Hao, J. Li, T. Yang, S. Yang, Understanding the doping effect on hydrogen evolution activity of transition-metal phosphides: modeled with Ni₂P, *Appl. Catal. B Environ.* 295 (2021), 120283.
- [56] Y. Jiao, Y. Zheng, K. Davey, S.Z. Qiao, Activity origin and catalyst design principles for electrocatalytic hydrogen evolution on heteroatom-doped graphene, *Nat. Energy* 1 (2016) 16130.
- [57] P. Chen, T. Zhou, L. Xing, K. Xu, Y. Tong, H. Xie, L. Zhang, W. Yan, W. Chu, C. Wu, Y. Xie, Atomically dispersed iron–nitrogen species as electrocatalysts for bifunctional oxygen evolution and reduction reactions, *Angew. Chem. Int. Ed.* 56 (2017) 610–614.
- [58] Y. Chen, R. Gao, S. Ji, H. Li, K. Tang, P. Jiang, H. Hu, Z. Zhang, H. Hao, Q. Qu, X. Liang, W. Chen, J. Dong, D. Wang, Y. Li, Atomic-level modulation of electronic density at cobalt single-atom sites derived from metal-organic frameworks: enhanced oxygen reduction performance, *Angew. Chem. Int. Ed.* 60 (2021) 3212–3221.
- [59] J. Yang, W. Li, D. Wang, Y. Li, Single-atom materials: small structures determine macroproperties, *Small Struct.* 2 (2021) 2000051.
- [60] J. Yang, W. Li, D. Wang, Y. Li, Electronic metal-support interaction of single-atom catalysts and applications in electrocatalysis, *Adv. Mater.* 32 (2020) 2003300.
- [61] Y. Yang, Y. Wang, H.-L. He, W. Yan, L. Fang, Y.-B. Zhang, Y. Qin, R. Long, X.-M. Zhang, X. Fan, Covalently connected Nb₄N_{5-x}O_x–MoS₂ heterocatalysts with desired electron density to boost hydrogen evolution, *ACS Nano* 14 (2020) 4925–4937.